Extreme Mechanics Letters 71 (2024) 102212

Contents lists available at ScienceDirect

Extreme Mechanics Letters

journal homepage: www.elsevier.com/locate/eml

# Role of friction and geometry in tuning the bending stiffness of topologically interlocking materials

Tracy Lu [a,1], Ziran Zhou [a,1], Punnathat Bordeenithikasem [b], Norman Chung [a], Diana Frias Franco [a], Jose E. Andrade [a], Chiara Daraio [a,*]

[a] Department of Mechanical and Civil Engineering, California Institute of Technology, 1200 E. California Blvd, Pasadena, 91106, CA, USA
[b] NASA Jet Propulsion Laboratory, California Institute of Technology, 4800 Oak Grove Dr, Pasadena, 91109, CA, USA

ARTICLE INFO

*Keywords:*
Tunable bending stiffness
Topologically interlocking materials
Woven architected materials
Level set discrete element method

ABSTRACT

Topologically interlocking material (TIM) systems offer adjustable bending stiffness controlled by external pre-stress, as shown in previous studies. This study focuses on a specific TIM system comprised of truncated tetrahedral particles interconnected via tensioned wires. The fabrication process involves weaving nylon wires through 3D printed truncated tetrahedrons that have longitudinal and latitudinal through-holes. By varying the tension applied to the wires, one can systematically control the overall bending stiffness of the TIM system. We change the surface friction and the contact angle between adjacent particles at a fixed wire tension, to study experimentally how they affect the system's bending response. We inform experiments with Level Set Discrete Element Method (LS-DEM) simulations, to correlate surface friction and contact area changes with the system's bending modulus. The numerical model is shown to be predictive and could be used in the future to evaluate designs of TIMs.

## 1. Introduction

The demand for materials with adjustable physical properties and the ability to respond rapidly to environmental stimuli has been growing [1]. In particular, fabrics with adaptable or tunable stiffness are applicable for use in soft robotics, shape morphing structures, and wearable devices [2–4]. For example, tunable fabrics can find use in wearable medical devices, like exoskeletons, haptic systems, and reconfigurable medical supports [5–7]. At larger scales, applications of tunable fabrics include transportable and reconfigurable architectures, which transition from a compact and flexible state to a deployed and rigid state [8,9].

Incorporating interlocking particles in fabrics opens up the possibility to incorporate added structural support and adjustable mechanical properties [10–13]. The mechanical behavior of such structured fabrics or topologically interlocking materials (TIM) is determined by the characteristics of their constituents and the topology of their arrangement [11,14–16]. In most architected materials and woven fabrics, these mechanical behaviors are determined during the design process and remain fixed after the components are fabricated. However, in some realizations, the fabric properties can be adjusted through actuation [13,17]. Wang, et al. demonstrated architected fabrics consisting of chain mail layers with interconnected particles, which demonstrate the ability to reversibly and gradually switch between soft and rigid states [2,16,17]. The control of the fabrics' stiffness is achieved by applying pressure at the boundary that jams the particles via vacuum suction, in a system similar to other structured fabrics [2,4,8]. While this example demonstrates the ability to create architected fabrics with tunable properties, the use of vacuum actuation is not practical, because it requires bulky and energy intensive pumping systems. Using tensioned fibers or artificial muscles could be a more compact and power-efficient solution [18].

In this paper, we study the response of a particular TIM system, consisting of truncated tetrahedral particles connected by woven tension wires [13,15,16]. Unlike the TIM system that is held solely by geometric interlocking and external in-plane constraint, which exhibits a softening stage before the TIM collapses [13], our fabric-TIM system shows a stiffening response during the indentation tests due to the gradual increment of anti-separation forces provided by the wires. The connecting wires facilitate the tunability of the bending modulus in response to adjustable applied tension, as demonstrated in Fig. 1c and d [16,17]. Additionally, they enable the formation of various flexible shapes while keeping the TIM structure intact. To better understand the fundamental mechanisms governing the tunability of the TIM system's apparent bending stiffness, we explore the role of contact angle and

* Corresponding author.
*E-mail address:* daraio@caltech.edu (C. Daraio).
[1] These authors contributed equally.

https://doi.org/10.1016/j.eml.2024.102212
Received 20 February 2024; Received in revised form 15 June 2024; Accepted 21 July 2024
Available online 25 July 2024

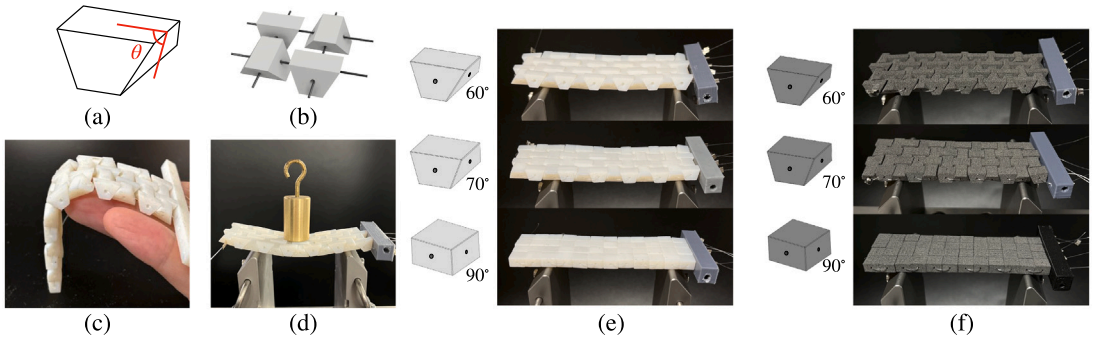


**Fig. 1.** (a) Schematic of a basic building block (particle) in the shape of a truncated tetrahedron [10], with dihedral angle, $\theta$, between the truncating surface and the side surface of particle; (b) Schematic of particles inter-connected by post-tensioned wires; (c) Unactuated, soft state of the sample; (d) Actuated, stiff state of the sample; (e–f) Samples made by particles with $\theta = 60°$, 70° and 90°; Samples shown in (e) are made by Vero White, with a measured friction coefficient of 0.2; samples shown in (f) are made by Nylon Polyamide 12, with a measured friction coefficient of 0.6.

contact friction at a fixed applied wire tension, using experiments and numerical simulations.

## 2. Design and fabrication of the topologically interlocking materials

There are various designs of TIMs. Dyskin, et al. [10] used tetrahedral solids to form layer-like structures that are interlocked topologically. Molotnikov, et al. [17] constructed TIM systems made of osteomorphic blocks embedded with shape memory alloy wires that can alter the TIM's flexural stiffness when activated. Siegmund et al. [16] created TIM systems using truncated tetrahedron blocks integrated with internal constraint fibers or woven tow material, demonstrating interlocking systems confined by passive elements.

Tetrahedrons are the simplest platonic solid, and all platonic solids can be arranged into layer-like structures in which they are interlocked topologically [19]. Additionally, trapezoidal particles are known for their substantial contact surfaces [12] and have extensive applications in architected materials to enhance mechanical performance [20]. Drawing inspiration from the previous references, we study a classic system of a TIM assembled with truncated tetrahedron particles as the basic building blocks (Fig. 1a). Using truncated tetrahedrons, as opposed to osteomorphic blocks, allows us to systematically change a single parameter, such as dihedral angle, to dictate the amount of interlocking. Moreover, since truncated tetrahedrons do not completely fit into each other, the relaxed state is more flexible and similar to a fabric. Inspired by Siegmund et al. [16], we design the particles with longitudinal and latitudinal through-holes. We use nylon wires to weave through each discrete particle and interconnect them, as depicted in Fig. 1b. To actuate the fabrics, we apply different levels of tension to the wires and thereby jam the particles with their neighbors to form an interlocked state (Fig. 1c–d). The combined outer surface of the truncated tetrahedrons upon post-tensioning is a flat plane. The resulting assemblies possess geometric contact and interlocking periodicity.

A series of TIMs were produced by varying two different particle parameters: the particle's dihedral angles, $\theta$ (Fig. 1a) and their surface friction. The particles were fabricated with three different dihedral angles, 60°, 70° and 90°, where the latter is simply a prism geometry with no geometric interlocking. To vary the surface friction, we 3D-printed the particles using two different materials of similar stiffness: Vero White (VW) using an Objet Stratasys Connex 500, and Nylon Polyamide 12 (PA12) using a Sintratec SLS 3D printer. Particles were cleaned by removing the outer support material. The Vero White particles were additionally cleaned in a 2 percent aqueous solution of NaOH to remove the remaining support material. The coefficients of friction were determined experimentally after the particles had been cleaned, using sliding friction tests. The resulting surface friction coefficients were measured to be 0.2 and 0.6, respectively. The particles were then woven together with 0.3 mm diameter nylon wire. The system is subsequently actuated with a small motor (28BYJ-48 Stepper Motor) that controls the amount of wire tension and therefore jamming the particles. A custom-designed fixture was 3D-printed for the motor housing and tensioning mechanism with sufficient clearance space for the tension meter (Checkline ETB-2000). The tension should attain the predetermined threshold, ensuring that the wire remains within the elastic range during the testing phase. The tension meter was used to gauge the tension and determine whether to incrementally increase the tension by spinning the motor. Once the desired average tension was achieved in the wires, the tension was secured with clamp beads to hold the wire in place. Then the woven sample was removed from the fixture with the motor.

## 3. Simulations

For a more systematic analysis of the TIM fabrics' behavior as a function of particle's geometry and constituent material properties, a reliable and validated numerical model is necessary. Level Set Discrete Element Method (LS-DEM) is used to model the physical experiment. LS-DEM is a variant of the traditional Discrete Element Method (DEM) allowing arbitrary object shapes. Originally developed for granular applications [21,22], LS-DEM has recently been adapted to study the structural behaviors of multi-block structures [23,24], and the structural analysis of TIM, showing satisfactory results in capturing the slip-governed failure [25,26] and the deflection limit [27] of the slab-like TIM. LS-DEM uses level set functions as the geometric basis, which calculates the signed distance $\phi$ from any arbitrary point in the space to the nearest surface of the grain. For example, in this work, a cross-sectional slice of a basic building block, which is the shape of a truncated tetrahedron, is a trapezoid in 2D, as shown in Fig. 2a. The surface of the building block, or particle, can be reconstructed by $\phi = 0$. We impose a set of surface nodes with uniform discretization size onto each particle (Fig. 2b). When checking potential particle contact, we take the position of each surface node $\mathbf{x}$ of one particle and check the corresponding level set value from another neighboring particle. If $\phi(\mathbf{x}) \leq 0$, then contact exists between this pair of particles.

Given the discrete nature of the woven-connected particles, LS-DEM is capable of extracting particle-scale information at micro-mechanical level, thus providing insight into how friction and contacts between particles affect the macroscopic property such as sample bending stiffness. Furthermore, the use of level set function provides flexibility in particle shape control, allowing us to easily simulate different particle shapes and investigate the combined geometric shape effects to the sample's overall behavior. The use of LS-DEM is also computationally efficient compared to other simulation methods such as finite element method (FEM) for potential simulations of large ensembles of particles [28].

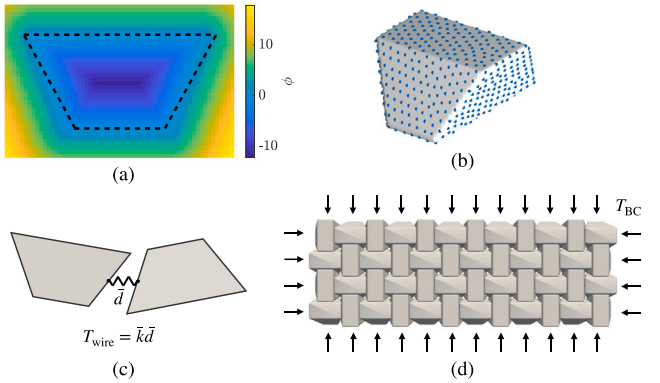


**Fig. 2.** (a) Illustration of the level set matrix of a slice of the truncated tetrahedron; (b) The particle is reconstructed by surfaces with $\phi = 0$; the imposed surface nodes are shown in blue dots; (c) Illustration of a pair of neighboring particles, connected by a massless spring with stiffness $\bar{k}$ and elongation $\bar{d}$; (d) Illustration of the sample under post-tensioning force $T_{\text{BC}}$. (For interpretation of the references to color in this figure legend, the reader is referred to the web version of this article.)

We use point forces acting on the boundary particles $T_{\text{BC}}$ to model the post-tensioning effect of the wires (Fig. 2d). On top of that, we use massless springs connecting the face center of the side of each particle to the face center of the side of its neighbors (Fig. 2c). The neutral position of the spring is at a distance $\bar{d} = 0$. The springs connecting neighboring particles can only exert tensile forces on the connected particles. When two neighboring particles are separated, the wire force $T_{\text{wire}}$ is calculated as

$$T_{\text{wire}} = \bar{k}\bar{d} \tag{1}$$

where $\bar{k}$ is the stiffness of the spring and is calibrated to match the experimental result of an uniaxial tension test carried out on a single woven wire.

## 4. Mechanical characterizations

In order to experimentally investigate the macroscopic properties of the sample under various particle geometries and material properties, displacement-controlled three-point bending tests were performed with an Instron E3000 Mechanical Testing Machine (Fig. 3a). The indenter had a set loading rate of 0.5 mm $s^{-1}$. To ensure that the TIM systems deform within their components' elastic limits, we imposed a maximum indentation depth of 5 mm. This indentation depth was determined by performing three-point bending tests on 3D-printed slabs of the same material with the same fabric sample dimensions. Tests show no yielding behavior within 5 mm. This indentation depth also guarantees that the wire remains within its elastic limit, confirmed by independent tensile tests on the wire, aligning with the assumption made in Eq. (1).

To compare the bending performance of the different fabrics, we define an apparent elastic bending modulus, $E^*$, as [2]:

$$E^* = \frac{KL^3}{4bh^3}. \tag{2}$$

Here, $K$ is the stiffness of the initial linear regime of the force–displacement plot obtained from the test machine, $L$ is the support span, $b$ is the width of the sample, and $h$ is the thickness of the sample before testing.

We study the role of friction and particle's shape on the overall fabric's behavior, comparing the apparent bending moduli values extracted from the experiments. Fig. 3b shows an overview of the bending modulus calculated from Fig. 3c–d using Eq. (2). Both increasing surface irregularities (i.e., friction between particles) and geometric interlocking have a positive correlation with the bending modulus. Samples made with PA12, resulting in a higher surface friction coefficient ($\mu$ = 0.6) than those made with Vero White (VW) ($\mu$ = 0.2), exhibit almost twice as much bending modulus as VW samples of the same particle geometry. Fig. 3c–d show the force–displacement plot for VW samples and PA12 samples accordingly. The force–displacement curves obtained from the three-point bending tests show an initially linear regime at small indentation depths, primarily due to the elastic response of the wire while the particles spread out. However, as the displacement increases, a nonlinear response is observed, most likely because of frictional sliding and local rearrangement of the particles within the system. Comparing the force–displacement plot within samples of the same material (Fig. 3c–d), we see that particles with smaller dihedral angle $\theta$, which result in higher interlocking upon post-tensioning, show higher stiffness. If we compare samples of same particle geometry but made with different materials, samples with higher surface friction show higher stiffness.

To construct the numerical model, we first construct the particles using level set functions and surface nodes (Fig. 2a–b). We then arrange and post-tension the particles (Fig. 2c–d), as described in Simulations section. To simulate the testing setup, we construct a 1:1 model of the experiment apparatus using the same level set technique (see Appendix). We then move the indenter downward at a constant loading rate. In the experiments, though the fabrics samples are prepared and post-tensioned according to the same procedure, there is no way to explicitly measure the slack of wires introduced during fabrication, and consequently it is not possible to know the exact tensile forces, $T_{\text{BC}}$, exerted by the wires on all particles. Therefore, we adjust the boundary force $T_{\text{BC}}$ in the bending simulation of the 70° VW sample until the simulated apparent bending modulus $E^*$ matches with that of the corresponding experiment. To ensure consistency and uniformity, we then apply the same calibrated boundary force to the remaining five simulations (60° and 90° VW samples, as well as 60°, 70° and 90° PA12 samples).

As depicted in Fig. 4, the resulting calibrated numerical model exhibits good agreement with experimental data regarding the apparent bending modulus $E^*$. In Fig. 4a, we show that as the friction coefficient reaches larger values (>∼0.3), the bending modulus of the samples does not increase as much, particularly for the samples with the least geometric interlocking (rectangular prism particles). As expected, in samples with more interlocked particles, the modulus increases more rapidly with increasing friction coefficient. For the 90° prism particles, the interwoven wire and friction between neighboring particles are the main factors that counteract out-of-plane deflection. With more interlocked particles (60° prism particles), however, not only friction and the wire, but also geometric constraints are collectively counteracting the out-of-plane deflection.

In order to analyze how geometry affects the modulus, we simulate the bending tests of samples made by 7 other particles of different degrees of geometric interlocking. Wang et al. [2] reported a quadratic law relating average particle contact number to the apparent bending modulus. In this work, since all particles are generated with surface nodes of uniform discretization size, the contact number per particle upon contact directly translates to contact area between the contacting neighboring particles. Since we are assuming a small indentation depth, we estimate the contact area to be the maximum area of the side surface of a truncated tetrahedron in contact with its neighbor at initial configuration before indentation, which is one trapezoid overlapped with a flipped trapezoid, or a hexagon. We plot the bending modulus against the normalized contact area projected onto the horizontal plane. Since the horizontal plane is directly perpendicular to the indenting direction, the projected horizontal contact area acts as the effective contact area for the solid material to counteract the indentation force. From Fig. 4b, we see that the bending modulus scales almost linearly with the horizontally projected contact area. The dihedral angle $\theta$ scales inverse-linearly with the bending modulus, due to the fact that particles with larger $\theta$ have smaller horizontal projected contact areas. From Fig. 4b

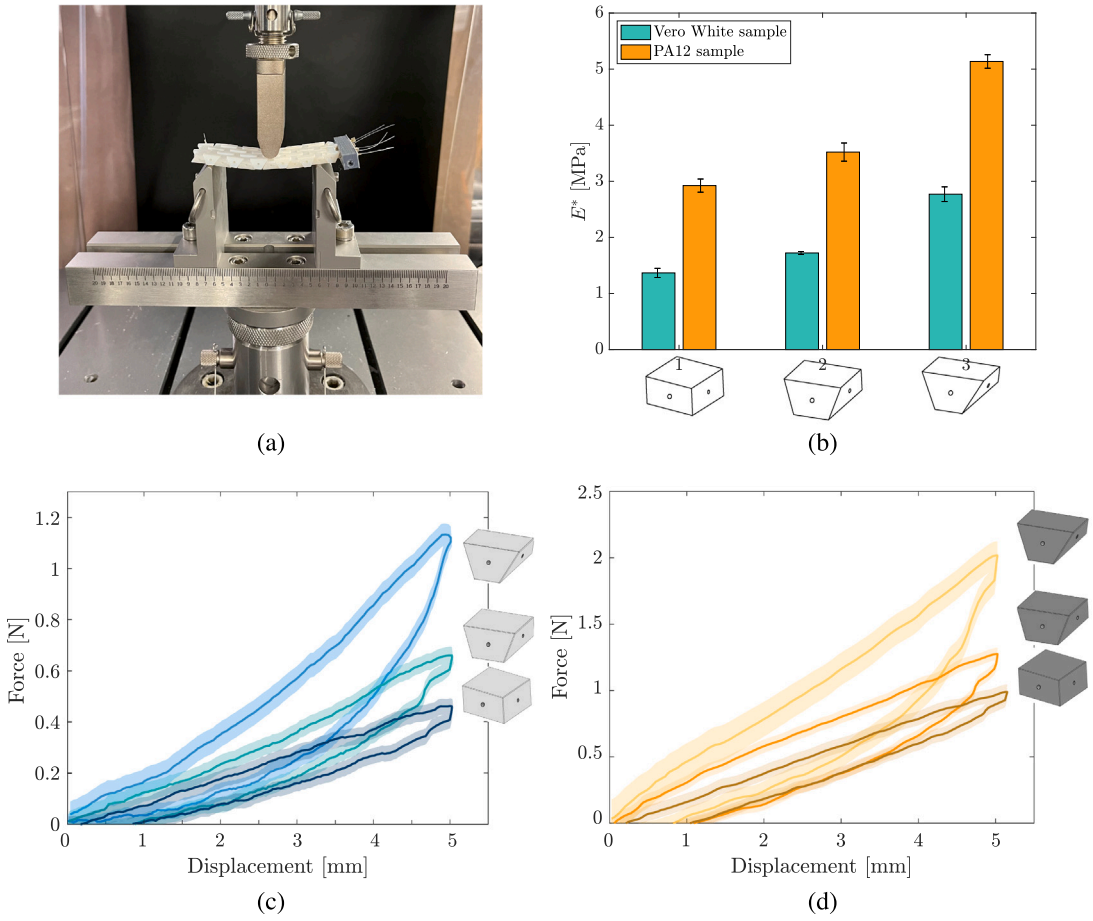


**Fig. 3.** (a) The three-point bending test setup with sample; (b) Apparent bending modulus of the different samples, fabricated with 2 different constitutive materials (Vero White and PA12) and three different dihedral angles ($\theta = 60°$, $70°$ and $90°$); (c) Force–displacement plots of the Vero White samples; (d) Force–displacement plot of the PA12 samples. In (c) and (d), for each sample, a total of five experiments are performed. The solid lines represent the average force–displacement behavior, and the shaded regions show the standard deviation over five experiments.

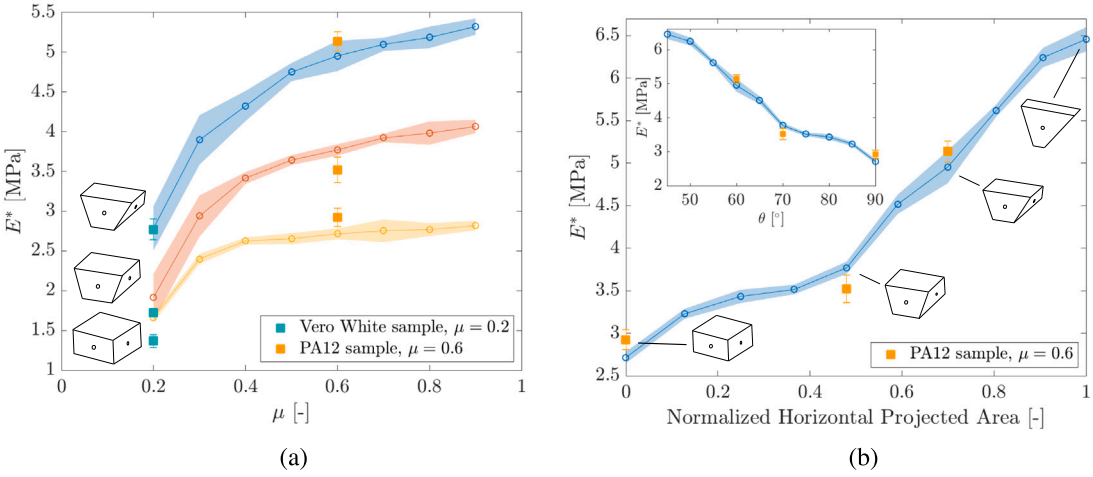


**Fig. 4.** Comparison of experiments and numerical simulations. (a) Simulated bending modulus of samples consisted of particles with $\theta = 60°$, $70°$ and $90°$ across different friction coefficient, from 0.2 to 0.9. For each particle shape at each friction coefficient, five simulations are run. For each run, noise is introduced to the initial particle position, particle orientation and boundary force $T_{BC}$. The solid line represents the average modulus, while the shaded regions show the standard deviation across five runs. Experiment results obtained from VW ($\mu = 0.2$) and PA12 ($\mu = 0.6$) samples are marked by green and orange respectively; (b) Simulated bending modulus vs. normalized contact area in horizontal projection with particles from $\theta = 45°$ to $\theta = 90°$ with $5°$ increments. The projected contact area is calculated based on the initial configuration of the particle orientation, and is normalized by the area of the $45°$ particle.
Inset: simulated bending modulus vs. $\theta$. Similar to (a), five simulations are run for each particle shape and noise is introduced in the initial state of each simulation. Experiment results from PA12 are marked in orange. (For interpretation of the references to color in this figure legend, the reader is referred to the web version of this article.)

and the additional inset figure, we see that particle geometry is a crucial factor in contributing to the bending modulus.

In contrast to [2], which exhibited a power law relationship, we find an approximately linear scaling between the projected horizontal contact area and the bending stiffness in our samples. We attribute this difference to the presence of the woven wires, which make the samples with less geometric interlocking rely more on elastic wire forces. During indentation, the wires in samples made from the rectangular prism particles are expected to be stretched more compared to samples made from the 45°-particles. This indicates that the wires may exert increased anti-separation forces within the 90°-particle TIMs in contrast to the other particles that can rely on greater geometric interlocking.

## 5. Conclusion

In this paper, we study the role of particles' geometry and inter-particle friction in the bending response of TIM systems consisting of truncated tetrahedron particles woven together with nylon wires. We fabricate samples with particles of varying interlocking contact angles and surface friction. In post-tensioned state, we find that both high friction and large horizontally projected contact area between the neighboring particles contribute positively to the resulting sample bending resistance. The positive effect of friction to bending stiffness diminishes as friction coefficient increases. The projected horizontal contact area positively contributes to the bending modulus at a linear rate.

The TIM is a complex system with many factors at play. Besides the friction and geometric interlocking, sample thickness and external post-stress also have profound effects on bending response. In order to isolate the effect of friction and geometry, we keep the sample thickness and post-stress consistent throughout all experiments and simulations. More comprehensive study on the combined effect of all factors should be investigated in future work.

## CRediT authorship contribution statement

**Tracy Lu:** Writing – review & editing, Writing – original draft, Visualization, Validation, Supervision, Software, Resources, Project administration, Methodology, Investigation, Funding acquisition, Formal analysis, Data curation, Conceptualization. **Ziran Zhou:** Writing – review & editing, Writing – original draft, Visualization, Validation, Supervision, Software, Resources, Project administration, Methodology, Investigation, Funding acquisition, Formal analysis, Data curation, Conceptualization. **Punnathat Bordeenithikasem:** Writing – review & editing, Supervision, Resources, Funding acquisition. **Norman Chung:** Validation, Software, Investigation, Formal analysis, Data curation. **Diana Frias Franco:** Validation, Software, Investigation, Formal analysis, Data curation. **Jose E. Andrade:** Writing – review & editing, Supervision, Resources, Project administration, Funding acquisition. **Chiara Daraio:** Writing – review & editing, Supervision, Resources, Project administration, Funding acquisition, Conceptualization.

## Declaration of competing interest

The authors declare the following financial interests/personal relationships which may be considered as potential competing interests: Chiara Daraio reports financial support was provided by Meta. Jose Andrade reports financial support was provided by National Science Foundation. Jose Andrade reports was provided by US Army Research Office. Punnathat Bordeenithikasem reports financial support was provided by Jet Propulsion Laboratory. Chiara Daraio was previously an Associate Editor for Extreme Mechanics Letters. If there are other authors, they declare that they have no known competing financial interests or personal relationships that could have appeared to influence the work reported in this paper.

**Table A.1**
Model parameters.

| Parameter | Value | Units |
|---|---|---|
| Normal particle stiffness $k_n$ | 2 | MN/m |
| Shear particle stiffness $k_s$ | 2 | MN/m |
| Wire stiffness $\bar{k}$ | 720 | N/m |
| Friction coefficient $\mu$ | {0.2,0.3,...,0.9} | – |
| Time-step $\Delta t$ | 5.6e−7 | s |
| Coefficient of restitution $C_{res}$ | 0.5 | – |

## Data availability

Data will be made available on request.

## Acknowledgments

Part of this research was done at the Jet Propulsion Laboratory (JPL), California Institute of Technology, USA, under contract with NASA (80NM0018D0004). This work was supported by the JPL Researchers on Campus program and Caltech President's and JPL Director's Research and Development Fund, USA. Reference herein to any specific commercial product, process, or service by trade name, trademark, manufacturer, or otherwise, does not constitute or imply its endorsement by the United States Government or the Jet Propulsion Laboratory, California Institute of Technology. J.E.A. and Z.Z. would like to acknowledge the support from the National Science Foundation (NSF), USA under award number CMMI-2033779, and the U.S. Army Research Office under grant number W911NF-19-1-0245.

## Appendix. Numerical model setup

Truncated tetrahedron particles are characterized by a level set grid of 2 mm/voxel. The surface nodes are discretized with a surface density of 230 points/cm$^2$. The contact mechanism of a pair of penetrating neighboring particles are estimated by visco-elastic models composed of linear springs and viscous dampers. The linear springs have normal and shear stiffnesses $k_n$ and $k_s$. The choice of these parameters takes into account factors considering material modulus and TIM arrangements, ensuring no excessive overlap between contacting particles [25]. We assume the stiffnesses of the particles made of two materials are comparable. The viscous dampers have normal damping coefficient $\gamma_n$ estimated based on coefficient of restitution $C_{res}$ [29] by

$$\gamma_n = 2\sqrt{mk_n}\frac{-\ln C_{res}}{\sqrt{\pi^2 + \ln {C_{res}}^2}}. \tag{A.1}$$

where $m$ is the mass of the particles. LS-DEM uses an explicit time integration scheme. The critical time-step is estimated by [30]

$$\Delta t = 0.4\sqrt{\frac{2m}{5k_s}}, \tag{A.2}$$

The wire stiffness $\bar{k}$ is calibrated to match the experimental result of a single woven wire in an uniaxial tension test. The set of parameters used in this work is documented in Table A.1.

We construct a 1:1 numerical model for the testing apparatus (Fig. A.5) with the same level set grid density and surface discretization density. The indenter and the two supports have the same dimension as the actual experimental test machine. The two supports are placed 6 cm apart, same as the experiment. After the numerical TIM sample has been post-tensioned, we allow the sample to settle onto the supports by gravity. We then move the indenter downward at a constant speed. Since we have a small time-step of $\Delta t = 5.6 \times 10^{-7}$ s for numerical stability, we apply a global damping parameter of $1 \times 10^{-4}/\Delta t$ s$^{-1}$ to ensure quasi-static conditions and to avoid excessive computation time [21].

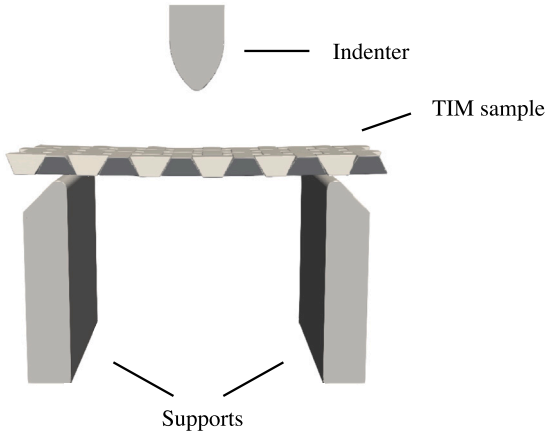


**Fig. A.5.** Numerical test apparatus.

## References


[1] M. Stoppa, A. Chiolerio, Wearable electronics and smart textiles: A critical review, Sensors 14 (7) (2014) 11957–11992, http://dx.doi.org/10.3390/s140711957, URL https://www.mdpi.com/1424-8220/14/7/11957.

[2] Y. Wang, L. Li, D. Hofmann, J. Andrade, C. Daraio, Structured fabrics with tunable mechanical properties, Nature 596 (2021) 238–243, http://dx.doi.org/10.1016/j.mechrescom.2018.07.002.

[3] S. Mondal, Phase change materials for smart textiles – an overview, Appl. Therm. Eng. 28 (11) (2008) 1536–1550, http://dx.doi.org/10.1016/j.applthermaleng.2007.08.009.

[4] D.S. Shah, E.J. Yang, M.C. Yuen, E.C. Huang, R. Kramer-Bottiglio, Jamming skins that control system rigidity from the surface, Adv. Funct. Mater. 31 (1) (2021) 2006915, http://dx.doi.org/10.1002/adfm.202006915.

[5] A.R. Ploszajski, R. Jackson, M. Ransley, M. Miodownik, 4D printing of magnetically functionalized chainmail for exoskeletal biomedical applications, MRS Adv. 4 (23) (2019) 1361–1366, http://dx.doi.org/10.1557/adv.2019.154.

[6] J.M. McCracken, B.R. Donovan, T.J. White, Materials as machines, Adv. Mater. 32 (20) (2020) 1906564, http://dx.doi.org/10.1002/adma.201906564.

[7] X. Yang, Z. Wang, B. Zhang, T. Chen, C. Linghu, K. Wu, G. Wang, H. Wang, Y. Wang, Self-sensing robotic structures from architectured particle assemblies, Adv.Intell. Syst. 5 (1) (2023) 2200250, http://dx.doi.org/10.1002/aisy.202200250.

[8] J. Ou, L. Yao, D. Tauber, J. Steimle, R. Niiyama, H. Ishii, JamSheets: Thin interfaces with tunable stiffness enabled by layer jamming, in: Proceedings of the 8th International Conference on Tangible, Embedded and Embodied Interaction, TEI '14, Association for Computing Machinery, New York, NY, USA, 2014, pp. 65–72, http://dx.doi.org/10.1145/2540930.2540971.

[9] P. Aejmelaeus-Lindström, J. Willmann, S. Tibbits, F. Gramazio, M. Kohler, Jammed architectural structures: Towards large-scale reversible construction, Granul. Matter 18 (2016) http://dx.doi.org/10.1007/s10035-016-0628-y.

[10] A. Dyskin, Y. Estrin, A. Kanel-Belov, E. Pasternak, A new concept in design of materials and structures: assemblies of interlocked tetrahedron-shaped elements, Scr. Mater. 44 (12) (2001) 2689–2694, http://dx.doi.org/10.1016/S1359-6462(01)00968-X.

[11] Y. Estrin, V.R. Krishnamurthy, E. Akleman, Design of architectured materials based on topological and geometrical interlocking, J. Mater. Res. Technol. 15 (2021) 1165–1178, http://dx.doi.org/10.1016/j.jmrt.2021.08.064.

[12] F. Barthelat, Architectured materials in engineering and biology: fabrication, structure, mechanics and performance, Int. Mater. Rev. 60 (8) (2015) 413–430, http://dx.doi.org/10.1179/1743280415Y.0000000008.

[13] S. Khandelwal, T. Siegmund, R.J. Cipra, J.S. Bolton, Adaptive mechanical properties of topologically interlocking material systems, Smart Mater. Struct. 24 (4) (2015) 045037, http://dx.doi.org/10.1088/0964-1726/24/4/045037.

[14] A. Molotnikov, R. Gerbrand, O. Bouaziz, Y. Estrin, Sandwich panels with a core segmented into topologically interlocked elements, Adv. Eng. Mater. 15 (8) (2013) 728–731.

[15] Y. Estrin, Y. Beygelzimer, R. Kulagin, P. Gumbsch, P. Fratzl, Y. Zhu, H. Hahn, Architecturing materials at mesoscale: some current trends, Mater. Res. Lett. 9 (10) (2021) 399–421, http://dx.doi.org/10.1080/21663831.2021.1961908.

[16] T. Siegmund, F. Barthelat, R. Cipra, E. Habtour, J. Riddick, Manufacture and Mechanics of Topologically Interlocked Material Assemblies, Appl. Mech. Rev. 68 (4) (2016) 040803, http://dx.doi.org/10.1115/1.4033967.

[17] A. Molotnikov, R. Gerbrand, Y. Qi, G.P. Simon, Y. Estrin, Design of responsive materials using topologically interlocked elements, Smart Mater. Struct. 24 (2) (2015) 025034, http://dx.doi.org/10.1088/0964-1726/24/2/025034.

[18] L. Wang, Y. Yang, Y. Chen, C. Majidi, F. Iida, E. Askounis, Q. Pei, Controllable and reversible tuning of material rigidity for robot applications, Mater. Today 21 (5) (2018) 563–576, http://dx.doi.org/10.1016/j.mattod.2017.10.010.

[19] A.V. Dyskin, Y. Estrin, A.J. Kanel-Belov, E. Pasternak, Topological interlocking of platonic solids: A way to new materials and structures, Phil. Mag. Lett. 83 (3) (2003) 197–203, http://dx.doi.org/10.1080/0950083031000065226.

[20] M. Weizmann, O. Amir, Y.J. Grobman, Topological interlocking in buildings: A case for the design and construction of floors, Autom. Constr. 72 (2016) 18–25, http://dx.doi.org/10.1016/j.autcon.2016.05.014, Computational and generative design for digital fabrication: Computer-Aided Architectural Design Research in Asia (CAADRIA).

[21] R. Kawamoto, E. Andò, G. Viggiani, J.E. Andrade, Level set discrete element method for three-dimensional computations with triaxial case study, J. Mech. Phys. Solids 91 (2016) 1–13, http://dx.doi.org/10.1016/j.jmps.2016.02.021.

[22] R.B. de Macedo, E. Andò, S. Joy, G. Viggiani, R.K. Pal, J. Parker, J.E. Andrade, Unearthing real-time 3D ant tunneling mechanics, Proc. Natl. Acad. Sci. 118 (36) (2021) http://dx.doi.org/10.1073/pnas.2102267118.

[23] J.M. Harmon, V. Gabuchian, A.J. Rosakis, J.P. Conte, J.I. Restrepo, A. Rodriguez, A. Nema, A.R. Pedretti, J.E. Andrade, Predicting the seismic behavior of multiblock tower structures using the level set discrete element method, Earthq. Eng. Struct. Dyn. 52 (9) (2023) 2577–2596, http://dx.doi.org/10.1002/eqe.3883.

[24] Z. Zhou, M. Andreini, L. Sironi, P. Lestuzzi, E. Andò, F. Dubois, D. Bolognini, F. Dacarro, J.E. Andrade, Discrete structural systems modeling: Benchmarking of LS-DEM and LMGC90 with seismic experiments, J. Eng. Mech. 149 (12) (2023) 04023097.

[25] S. Feldfogel, K. Karapiperis, J. Andrade, D.S. Kammer, Failure of topologically interlocked structures — a level-set-DEM approach, Eur. J. Mech. A Solids 103 (2024) 105156, http://dx.doi.org/10.1016/j.euromechsol.2023.105156.

[26] S. Feldfogel, K. Karapiperis, J. Andrade, D.S. Kammer, Scaling, saturation, and upper bounds in the failure of topologically interlocked structures, Int. J. Solids Struct. 269 (2023) 112228, http://dx.doi.org/10.1016/j.ijsolstr.2023.112228.

[27] S. Ullmann, D.S. Kammer, S. Feldfogel, The Deflection Limit of Slab-Like Topologically Interlocked Structures, J. Appl. Mech. 91 (2) (2023) 021004.

[28] A.S. Dalaq, F. Barthelat, Manipulating the geometry of architectured beams for maximum toughness and strength, Mater. Des. 194 (2020) 108889.

[29] Y. Tsuji, T. Kawaguchi, T. Tanaka, Discrete particle simulation of two-dimensional fluidized bed, Powder Technol. 77 (1) (1993) 79–87, http://dx.doi.org/10.1016/0032-5910(93)85010-7.

[30] X. Tu, J.E. Andrade, Criteria for static equilibrium in particulate mechanics computations, Internat. J. Numer. Methods Engrg. 75 (13) (2008) 1581–1606, http://dx.doi.org/10.1002/nme.2322.